

EPJ D

Atomic, Molecular,
Optical and Plasma Physics

EPJ.org

your physics journal

Eur. Phys. J. D **63**, 431–440 (2011)

DOI: 10.1140/epjd/e2011-20077-4

Determination of sheath parameters by test particles upon local electrode bias and plasma switching

G. Schubert, R. Basner, H. Kersten and H. Fehske



Determination of sheath parameters by test particles upon local electrode bias and plasma switching

G. Schubert^{1,2}, R. Basner³, H. Kersten^{4,a}, and H. Fehske¹

¹ Institut für Physik, Ernst-Moritz-Arndt-Universität Greifswald, Germany

² Regionales Rechenzentrum Erlangen, Friedrich-Alexander-Universität Erlangen-Nürnberg, Germany

³ Leibniz-Institute for Plasma Research and Technology (INP) Greifswald, Germany

⁴ Institute for Experimental and Applied Physics, University of Kiel, Germany

Received 31 January 2011 / Received in final form 5 May 2011

Published online 28 June 2011 – © EDP Sciences, Società Italiana di Fisica, Springer-Verlag 2011

Abstract. Equilibrating gravitation by electric forces, microparticles can be confined in the plasma sheath above suitably biased local electrodes. Their position depends on the detailed structure of the plasma sheath and on the charge that the particles acquire in the surrounding plasma, that is by the electron and ion currents towards it. Bias switching experiments reveal how the charge and equilibrium position of the microparticle change upon altered sheath conditions. Above a critical bias, the particle is subject to an additional downward acceleration that cannot be explained solely by gravity and ion drag. This acceleration can be attributed to a positive charging of the particle induced by extreme out-of-equilibrium conditions of the plasma sheath in its surroundings: locally the plasma sheath can be completely deprived of electrons by means of the bias. We observe similar particle behaviors also in the afterglow of the discharge for a persisting bias voltage on the electrode: damped oscillation into a new equilibrium or (accelerated) fall according to the bias. The observed particle dynamics in locally tailored plasma sheath environments directly monitors changes in electric field structures and plasma density profiles.

1 Introduction

At the powered electrode of an asymmetric rf-discharge, self biasing gives rise to a large potential drop, wide plasma sheath and strong electric fields. In contrast, the plasma sheath in front of grounded or weakly biased electrodes is less pronounced and thinner. The properties of such sheaths are, nevertheless, of fundamental interest in view of technological plasma processing of surfaces [1,2] and plasma chemistry [3]. Rf-discharges with additionally biased substrates are often used in thin film magnetron sputtering or physically enhanced chemical vapor deposition. In particular, the space charge sheath region adjacent to the surfaces has been the subject of much investigation. As the ions required for etching of semiconductors gain their energy from the fields within the sheath, knowledge of the spatial variation of these fields is important for the best design of manufacturing processes. Along this line, selective local biasing of the substrate can be used to optimize the electron and ion impact energies and directions [4]. Moreover, such an experimental realization provides a possibility for the evidence of an exclusive ion current to the substrate surface. On the other hand, one can influence the transport of particulates in plasma by

suitable local switching of bias voltages in order to manipulate the dust particles [5]. With respect to particle formation and confinement as well as to avoid undesired transport it is also of great interest to study the behavior of the particles if the plasma is switched off.

Monitoring potentials and densities or temperatures of the species in the sheath is challenging, since common diagnostics, such as Langmuir-probes usually fail. This is because the macroscopic tip of a Langmuir-probe significantly alters the local plasma characteristics and cannot resolve density and potential gradients in the narrow sheath with adequate precision. In order to overcome these limitations, alternative diagnostics like optical spectroscopy [6,7] or microparticles as probes [8,9] are used. If dust particles are injected into a plasma, they become negatively charged and confined in the discharge. The trapping is due to the balance of the forces acting on the particles. By observing the position and movement of the particles in dependence on the discharge parameters, information can be obtained on the electric field in front of electrodes and substrate surfaces where other plasma diagnostic methods fail [10]. Test particles provide an efficient, nearly non-invasive tool for the local diagnostic of the sheath parameters. Most experiments [10,11] focus onto sheaths in front of rf-driven electrodes where the

^a e-mail: kersten@physik.uni-kiel.de

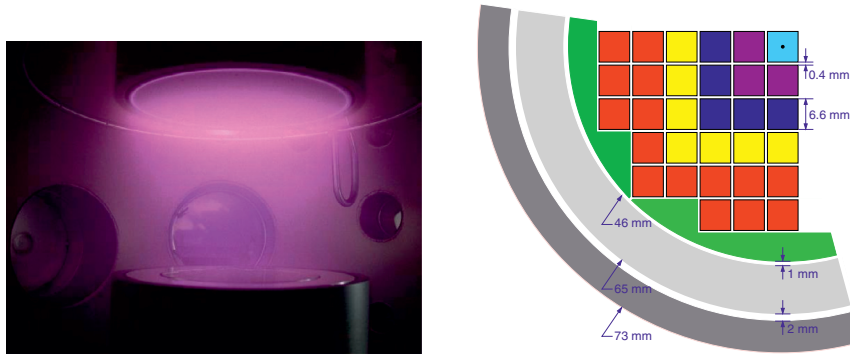


Fig. 1. (Color online) Left panel: powered (top) and adaptive (bottom) electrode of the PULVA-INP device during operation of an argon plasma. Right panel: design of the adaptive electrode (only a representative part of the AE is shown). From the center outward: square pixels, fitting segments (green), ring (light grey) and ground shield (dark grey). The spacings between all constituents are isolating.

electric field is rather strong, or onto global changes of the plasma properties. In our study we confined the test particles in front of an adaptive electrode (AE) where the sheath can be influenced locally and additional bias voltages can be applied [8,9]. Furthermore, we investigated the particle behavior not only during the presence of the plasma, but even in the temporal afterglow of the plasma. These experiments provide insight into typical situations which occur in process plasmas for particle manipulation and powder handling. In view of their practical use, a calibration is necessary to discern their own charge dynamics from their capability to reflect the properties of the surrounding plasma.

Upon immersion in a plasma, microparticles get charged by electrons and ions that accumulate on their surface. Since the electron mobility exceeds those of the ions, the particle charge is in general negative, depending on the local conditions of the surrounding plasma. Albeit, it has been stressed that under certain conditions, such as in a discharge afterglow, microparticles in the bulk plasma can even acquire positive charges [12]. While the plasma is operational, particle recharging takes place on longer time scales than the almost instantaneous reaction of the plasma to slightly modified external conditions. Then, the particle charge constantly remains in equilibrium with the surrounding electrons and ions. Drastic changes in the operating conditions, however, may perturb the time scale ordering and hinder an equilibration of the particle charge. As a consequence of a strongly perturbed environment, a discharging or even positive charging of the particle becomes possible in such out-of-equilibrium situations.

In this work, we investigate microparticles which are captured in the plasma sheath above a grounded or weakly biased electrode and their reaction to changes in the operating conditions of the plasma. Thereby, we focus on switching off the plasma while retaining the biasing of the electrode as well as changing the bias voltage during operation of the plasma. The experimental results are discussed in view of a theoretical model that combines basic equations with input data from particle-in-cell (PIC) simulations.

2 Experimental setup

The PULVA-INP setup [13] consists of an asymmetric, capacitively coupled rf-plasma in argon, working at neutral gas pressures p_{Ar} from 0.1 Pa to 100 Pa. The reactor possesses an upper (rf-driven) electrode and a bottom (grounded or weakly biased) electrode with 101 square pixels, which can be biased independently by dc-voltages. The rf-power (P_{rf} [W] = 5–100) is supplied by the upper, powered electrode at a frequency of $\nu_{rf} = 13.56$ MHz and amplitudes Φ_{rf} up to 1000 V. In dependence on the external parameters P_{rf} and p_{Ar} , the obtained characteristics for the pristine argon plasma are electron densities n_e [cm⁻³] = 10⁹–10¹¹, electron energies $k_B T_e$ [eV] = 0.8–2.8 and plasma potentials with respect to the ground of Φ_p [V] = 20–30 [14]. Electron parameters are measured by Langmuir probe measurements whereas the ionic parameters such as flux densities and ion energy distribution are monitored by energy-resolved mass spectrometry (plasma monitoring).

The key feature of the experimental setup is the lower, so called ‘adaptive’ electrode (AE; see Fig. 1 left-hand panel). It consists of 101 square electrode segments (pixels) with a linear extension of 6.6 mm each, separated by thin (0.4 mm) isolating gaps (see Fig. 1 right-hand panel). In addition, four larger segments fit the pixel geometry to the surrounding ring and ground shield. All 105 electrode pixels can be biased individually or in groups by an external dc-voltage of up to $\Phi_{bias} = \pm 100$ V. The selective application of bias voltages to some pixels allows for studying spatial and temporal changes of the plasma sheath [8,13]. The small extension of the pixels as compared to the remaining grounded electrode guarantees that the applied bias only locally influences the plasma sheath but leaves the overall discharge conditions unaltered.

All experiments in this work refer to a plasma operating power $P_{rf} = 10$ W and neutral gas pressure $p_{Ar} = 5$ Pa unless stated differently. The microparticles used as probes are melamine-formaldehyde (MF) spheres with diameter $d = 9.6$ μ m. With a mass density of $\rho_m = 1.51 \times 10^3$ kg m⁻³ for MF this results in a particle mass of $m = 7 \times 10^{-13}$ kg. Illuminated by a laser fan (532 nm), their positions are

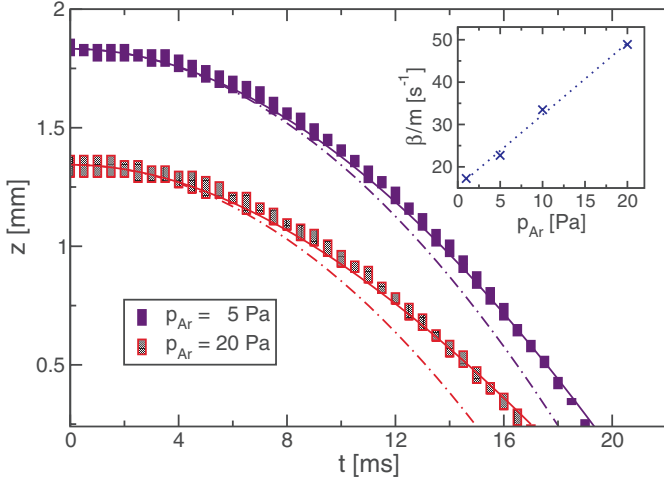


Fig. 2. (Color online) Main panel: measured vertical particle position after switching off the plasma for different neutral gas pressure p_{Ar} (boxes). Theoretical trajectories for freely falling [retarded by friction according to (1)] particles are given by dashed-dotted (solid) lines. Inset: crosses give the friction coefficient β/m as extracted from fitting (1) to the experimental data. The dotted line is a guide to the eye.

recorded by a fast CCD camera (up to 2000 frames per second, e.g. exposure time was 0.5 ms).

3 Results and discussion

In this work we report on three different experiments. Each one describes a particular way in which the equilibrium conditions for a levitated particle in the plasma sheath are perturbed. The initial position of the particle is determined by an equilibrium between gravitational and electrostatic forces. Neutral drag and thermophoresis effects are negligible. The effect of ion drag forces will be discussed in the experiments for which it is relevant.

3.1 Plasma afterglow – unbiased adaptive electrode

In this experiment we start from an initial configuration where the MF-particle is trapped above the unbiased center pixel by a confining potential of -5 V on the surrounding pixels of the AE. At $p_{\text{Ar}} = 5\text{ Pa}$, the sheath width is about 3 mm and the equilibrium position $z_0 = 1.8\text{ mm}$. Switching off the plasma, the electrostatic force no longer compensates gravity and the particle drops onto the AE. As compared to a freely falling particle, the drop is markedly retarded (see Fig. 2).

Along with the residual electric field, which decays over some μs , also the directed ion current towards the AE vanishes and ion drag can be neglected. The only forces relevant on the time scale of the fall (ms) are gravitation $\mathbf{F}_g = -mge_z$ and neutral drag force $\mathbf{F}_n = -\beta\dot{\mathbf{z}} = -\beta\dot{z}e_z$. Here the damping constant β depends on the local density of the background gas, which we assume to be constant in

time. Then the equation of motion for the particle reads $\ddot{z} + \frac{\beta}{m}\dot{z} + g = 0$. The solution of this equation, subject to the initial conditions $\dot{z}(t=0) = 0$ and $z(t=0) = z_0$ is given by

$$z(\tau) = z_0 + \frac{m^2g}{\beta^2} (1 - e^{-\tau} - \tau), \quad (1)$$

where we introduced the normalized time $\tau = \beta t/m$. Depending on the argon gas pressure, the values of β/m obtained by a least squares fit of (1) to the experimental data are in the range of 20 s^{-1} to 50 s^{-1} . This so called Epstein friction coefficient [15] can be related to the neutral gas pressure by

$$\frac{\beta}{m} = \delta \frac{8}{\pi} \frac{p_{\text{Ar}}}{\rho_m v_{\text{Ar}}^{\text{th}} d/2}, \quad (2)$$

where $v_{\text{Ar}}^{\text{th}}$ is the thermal velocity of the argon gas atoms and δ is a parameter in the order of 1–1.5 accounting for how the gas atoms are deflected from the particle surface [16]. Assuming a diffuse reflection, we obtain a theoretical value of $\beta/m \sim 30\text{ s}^{-1}$ for $p_{\text{Ar}} = 20\text{ Pa}$ at room temperature, which is in good accordance with the values determined by the measurement. Furthermore, to describe our experimental data it is not necessary to adapt β to the decaying neutral gas density in the discharge afterglow, as discussed in reference [12]. Within our accuracy a constant value of β is sufficient. For lower gas pressure values the damping constant significantly deviates from the Epstein law since the delayed charging effect becomes dominant [17]. Due to the vanishing electric field this experiment does not provide any information on the value or variation of the particle charge. In order to obtain information on this aspect, we have to resort to a slightly modified setup, retaining a static dc-bias at some pixels of the AE.

3.2 Plasma afterglow – biased adaptive electrode

Extending the previous experiment, we start from various bias configurations of the AE by which we initially trap a particle. Clearly, the biased pixels locally warp the plasma sheath. Thus, the equilibrium positions (and presumably also the charges) of the particles differ for each case. The configurations for which the results are given in Figure 3 differ in the number of biased pixels – (3×3) for the left and (5×5) for the right panel, respectively. The applied bias voltages exhaust the available range of voltages provided by the AE, resulting in weak to strong confinement. For weak confinement ($|U_{\text{dc}}| < 60\text{ V}$) we recover in the left panel of Figure 3 the falling behavior observed in the previous experiment. Only for stronger negative bias ($|U_{\text{dc}}| \geq 60\text{ V}$) the persisting electric field is strong enough to keep the particle hovering above the AE. Note that the lengths of the recorded time intervals are limited by the particle horizontally leaving the camera focus. Their levitating state persists over several seconds. The particle trajectories in the right panel of Figure 3 are

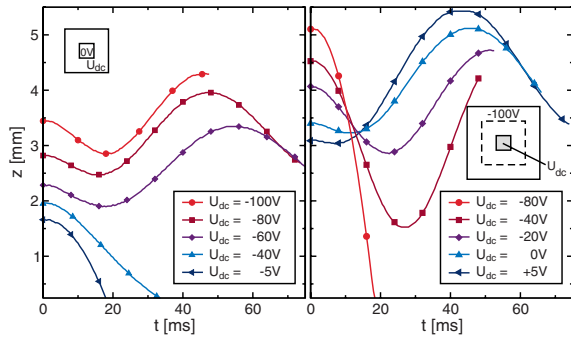


Fig. 3. (Color online) Measured vertical particle position after switching off the plasma while retaining dc-biases on selected segments of the AE. Left panel: bias voltages $U_{AE} = (0, U_{dc}, 0)$, where the three numbers refer to the pixel biasing from the center of the AE outward – (light blue, violet, dark blue) with pixel colors referring to Figure 1. The rest of the AE is grounded. Right panel: Bias voltages $U_{AE} = (U_{dc}, -100\text{ V}, -100\text{ V})$. Time resolution of the measurement is 0.5 ms and symbols are given to distinguish the curves. Error bars for the positions are comparable to the symbol size.

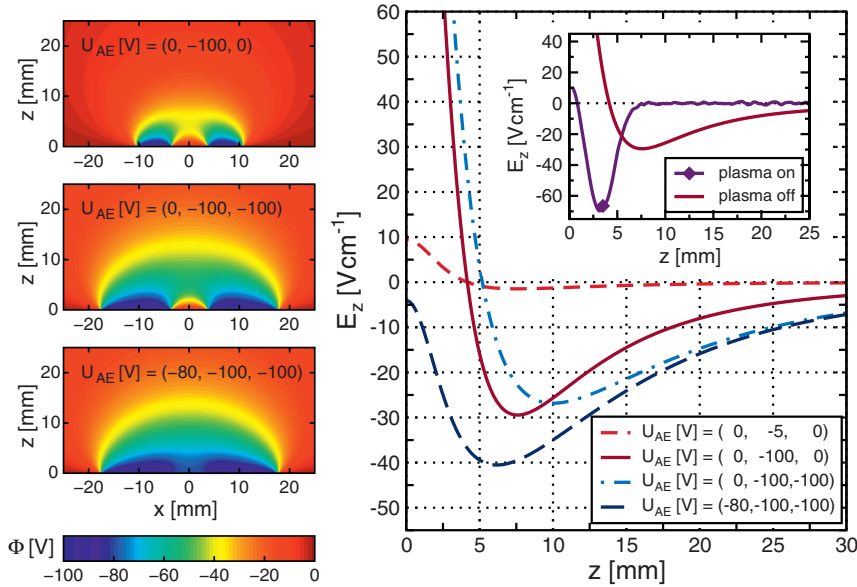


Fig. 4. (Color online) Left panel: vertical cut through the electrostatic potential distribution above the AE in absence of any plasma. The shown region depicts only a fraction of the calculation grid ($n_x \times n_z = 1400 \times 2000$ grid points corresponding to $7\text{ cm} \times 10\text{ cm}$, $x \geq 0$). Right panel: vertical component of the electric field on the symmetry axis as extracted from the potential data. In the inset the electric field for $U_{AE}[\text{V}] = (0, -100, 0)$ before and after switching off the plasma is given. The data for operating plasma result from a PIC simulation. The diamond indicates the measured initial equilibrium position of the particle.

shifted to markedly larger distances from the AE. This reflects the more pronounced widening of the plasma sheath by the larger area of strongly biased pixels. As long as the surrounding pixels are on a sufficiently negative bias, the particle levitation even persists for a moderate positive voltage on the center pixel. For a large negative bias ($U_{dc} = -80\text{ V}$), however, switching off the plasma causes an abrupt drop of the particle, which is even accelerated as compared to a free fall.

In order to explain the observed behavior, a first idea would be to assume that on the observed time scales the plasma has completely decayed, i.e. all electrons and ions have already recombined. Then, the particle trajectory corresponds to the motion of a charged sphere between two parallel plates, that are the powered electrode and the AE. Using the superposition principle, we may calculate the electrostatic force acting on the particle in two steps. First, the self-force for a charged particle between two parallel, grounded planes is calculated analytically by means of an infinite series of image charges [18] (see Appendix A). This contribution is, however, negligible for distances $z \gtrsim 0.1\text{ mm}$. Second, we numerically solve the boundary value problem and calculate the potential due to the biased electrode pixels. To this end, we reduce the simulation volume to a two-dimensional, cylindrically symmetric domain by smearing out the individual pixels

to rings, and use routines from FISHPACK [19]. In vertical direction the simulation volume covers the whole range between both electrodes. Radially, the simulation domain is such large that the boundaries do not affect the results near the center of the discharge. At r_{max} we used vanishing radial field boundary conditions.

Due to rotational symmetry, the biasing of outer lying pixels influences the electrostatic potential above the center pixel to the point of generating a region with negative potential at finite z (left panel of Fig. 4). Above an unbiased center pixel this gives rise to a potential structure with a minimum at z_0 . For strong negative biasing of the center pixel, $U_{AE}[\text{V}] = (-80, -100, -100)$, the potential along the symmetry axis monotonically increases with z . The sign change of the electric field at z_0 implies that a negatively charged particle may only remain hovering for $z > z_0$ since there gravity and electrostatic force are antiparallel (right panel of Fig. 4). As compared to the case of operating plasma, the electric field after the switching off is markedly reduced (inset of the right panel of Fig. 4). Therefore, keeping up the force equilibrium requires an increasing of the particle charge. Whether the particle remains hovering or drops down onto the AE depends on its ability to collect enough negative charges from its surroundings. Here the time scale ordering of particle recharging and plasma decay are of major importance. A particle

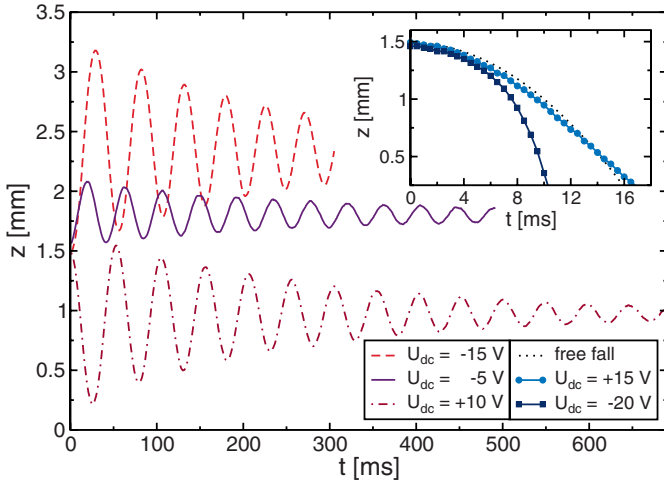


Fig. 5. (Color online) Measured vertical particle position upon bias switching while the plasma is kept operational. The initial confining potential is $U_{\text{AE}}[\text{V}] = (0, -5, -50)$, which is switched to the final configuration $U_{\text{AE}} = (U_{\text{dc}}, U_{\text{dc}}, -50 \text{ V})$. In the inset the time scale is magnified to resolve the dynamics of those particles that drop onto the AE. For comparison the trajectory of a freely falling particle is given.

adapts its charge to altered electron- and ion densities in its surrounding within some $1\text{--}10 \mu\text{s}$ [20]. The relevant stages of a plasma decay and the associated time scales have also been investigated in the literature. Couédel et al. [12] focussed on the bulk properties at higher operating pressures, while Osiac et al. [21] studied the plasma sheath in the afterglow of a pulsed inductively coupled rf-plasma in hydrogen. From their time scale estimates we may argue that the particle charge adiabatically adapts to the altered conditions during the early stages of the plasma decay. In the late afterglow, however, a residual particle charge ‘freezes out’ since low electron and ion densities do not allow for an equilibration anymore [12]. Thereafter (on the time scale of ms), the particle dynamics can be described as the movement of a charged particle in an external electrostatic potential, justifying our initial assumption. In contrast to the reasoning by Couédel et al. in our experiment local electron and ion densities differ significantly for all times due to sheath structure and additional biasing. Therefore, also markedly higher particle charges are possible. While ambipolar diffusion is the dominant transport mechanism in the plasma afterglow, the electron and ion currents are locally deviated by the persisting bias on the AE-pixels. Upon a strong negative bias, this may cause the vicinity of the particle to be completely deprived of electrons since the periodic electron flooding of the sheath in each rf-cycle ceases. Then the sole presence of ions will drastically reduce the negative charge of the particle, eventually to the point of a positive recharging. This might explain the observed accelerated fall for $U_{\text{AE}}[\text{V}] = (-80, -100, -100)$, which cannot be attributed to gravity and ion drag force [22–24] alone. In order to discern the contributions to the total force acting on the particle, we resort to a bias switching experiment in the next section. While the observed particle

behaviors in both experiments are similar, the persisting plasma permits a reliable calculation of the final plasma properties by particle-in-cell simulations.

3.3 Persisting plasma – bias switching

In the plasma afterglow the plasma conditions change on time scales of some $10 \dots 100 \mu\text{s}$ [21]. This is in contrast to the situation where the AE-pixel biasing is switched during operation of the plasma. Here, the local plasma sheath adapts within 1–5 rf-cycles to the new biasing configuration and thus has an instantaneous impact on the charge and force equilibrium of the particle. In principle, a particle may be trapped into a stable equilibrium position for all indicated biasing configurations in Figure 5, provided that the relaxation is performed smoothly. Upon an abrupt change from an initial configuration, however, the particle drops onto the AE outside a rather narrow region of bias variations (see inset of Fig. 5). This holds for either positive or negative voltages. Interestingly, again a strong negative bias leads to an acceleration of the particle towards the AE which is not explicable solely by gravity. For moderate changes in the biasing configuration the particle reaches its new equilibrium position through a damped oscillatory motion.

In order to describe the different behaviors quantitatively, we performed a PIC-simulation of the plasma discharge. Special emphasis is put on the local modifications of the plasma sheath by the AE-pixels. Details on the simulation can be found in Appendix B.

The initial AE-configuration in Figure 5 only marginally disturbs the plasma sheath above the center pixel. Its primary purpose is to keep the particle in the camera focus. As can be seen from the simulation results in Figure 6, both the electron and ion densities near the symmetry axis agree with those in the unperturbed sheath far away from the biased pixels. In this respect, the results for $U_{\text{AE}}[\text{V}] = (0, -5, -50)$ in Figure 7 are representative for an unperturbed sheath. While the two-dimensional color plots in Figure 6 provide a general overview of the sheath structure above the AE-pixels, Figure 7 allows for a quantitative analysis on the symmetry axis. The time-averaged electron density is markedly reduced as compared to the ion density. Electrons may overcome the potential barrier of the plasma potential and enter the sheath only during a short fraction of an rf-period. This occurs, when the potential on the powered electrode is sufficiently negative to supply enough kinetic energy to the electrons. Upon additional negative biasing of an AE-pixel, the necessary energy for crossing the sheath increases. This results in a further reduction of the electron density since for most electrons the sheath becomes impenetrable. Having lost their kinetic energy already after some part of the sheath, they remain trapped in the plasma. Hence, above the negatively biased pixel, parts of the sheath may be completely deprived of electrons. Because of the continuity equation and acceleration of the ions towards the AE, their (time-averaged) density also decreases in the sheath. Their larger mass makes them less susceptible to further acceleration

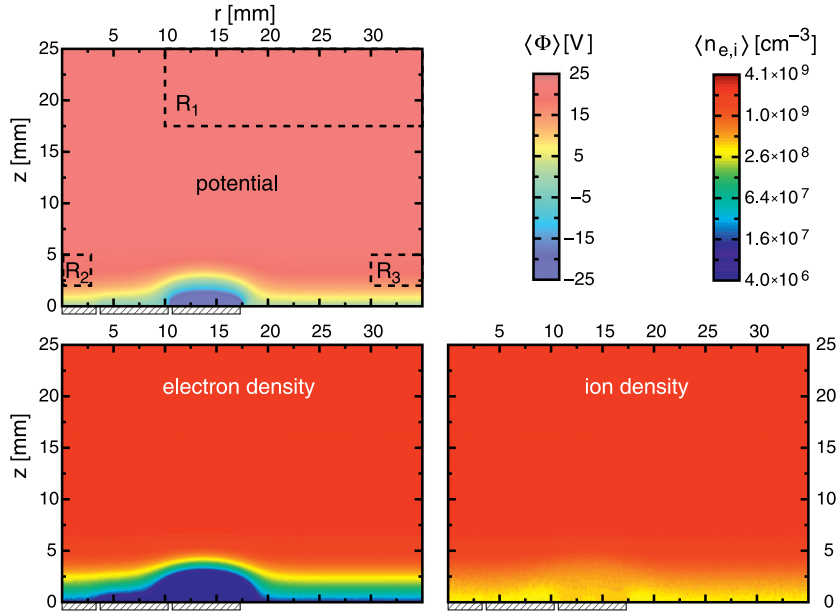


Fig. 6. (Color online) PIC-results for the time-averaged potential as well as electron and ion density. Only part of the total simulation volume is shown. The AE-pixels are indicated by hatched rectangles and the biasing corresponds to the initial configuration in Figure 5. In the upper panel $R_1 - R_3$ indicate the diagnostic regions for which the local electron energy probability distributions are given in Figure 8.

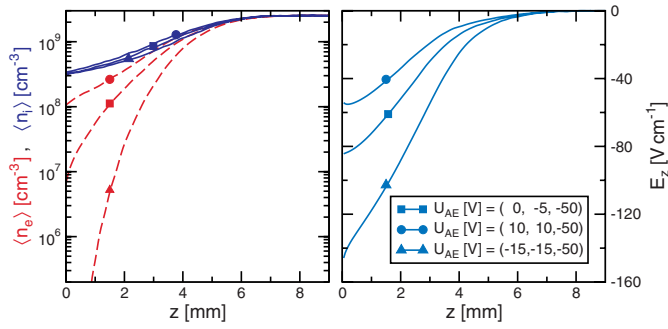


Fig. 7. Influence of the pixel biasing on electric field as well as electron and ion density on the symmetry axis of the discharge. Results obtained by PIC simulation.

by additional biasing and therefore all ion densities nearly coincide. In contrast to switching off the plasma, which leads to wider final potential structures and weaker fields, a negative bias may drastically enhance the electric field in the sheath. This enhancement results from the dominance of the increased potential difference over the effect of sheath widening.

The density profile does not contain any information on the energy of the electrons in the sheath. Therefore, we calculate the electron energy probability distribution $g_p(E)$ [4]. In Figure 8 $g_p(E)$ is given for three regions of the discharge, representing bulk, unperturbed sheath and sheath above a biased electrode pixel. The scales used in Figure 8 are chosen such that a Maxwellian distribution results in a straight line. Then the electron temperature is proportional to the inverse slope and the crossing with the ordinate gives the species density. The obtained $g_p(E)$ for the bulk closely resembles a bi-Maxwellian distribution with a larger fraction of cold and a smaller fraction of higher energetic electrons. The latter one is due to those electrons that oscillate between the electrodes of the dis-

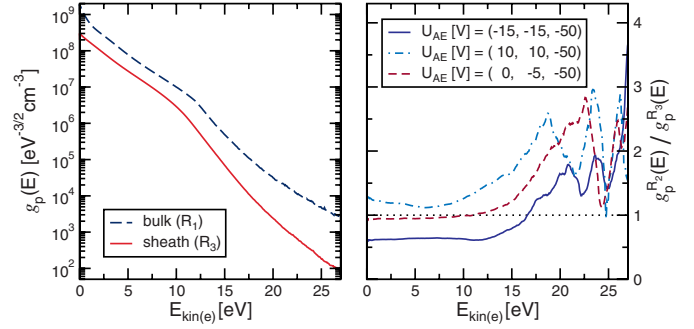


Fig. 8. (Color online) Left panel: PIC results for the local electron energy probability function $g_p(E)$ in the bulk and the sheath of the discharge. Right panel: changes in $g_p(E)$ above the center AE-pixel induced by different biasing. Away from the biased pixels, the EEPF in region R_3 agrees for all AE configurations.

charge. In the sheath, the density is reduced for all energies, but most pronounced in the high energy tail. This is due to the retardation caused by the potential difference the electrons encounter when crossing the sheath. As compared to the unperturbed sheath, $g_p(E)$ above the center pixel clearly reflects the influence of the additional AE-biasing (right panel of Fig. 8). For energies up to the plasma potential, the density reduction (enhancement) for negative (positive) bias is uniform for all energies. The strong fluctuations at larger energies are due to poor statistics since only a tiny fraction of all electrons have energies in this range. Irrespective of the biasing on the center pixel, the confinement potential on the third shell of pixels increases the density in the high energy tail as compared to the unperturbed sheath through a channeling effect.

Explaining the accelerated fall of the particle quantitatively requires a careful analysis of all relevant forces. In order to extract the total force on the particle from the

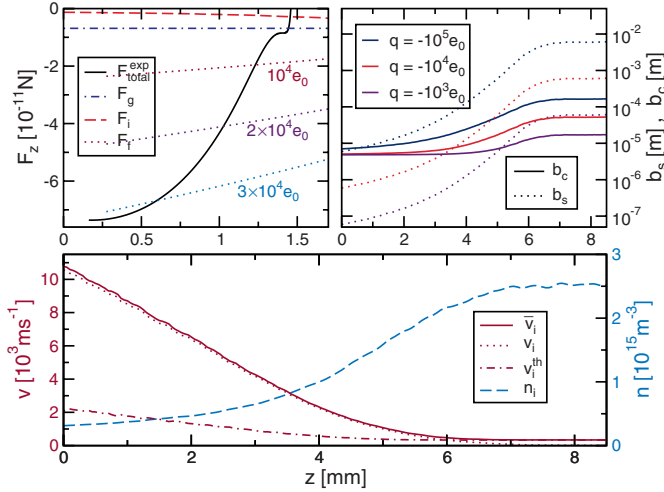


Fig. 9. (Color online) Upper left panel: total force $F_{\text{total}}^{\text{exp}}$ on the particle as extracted from the experimental trajectory. Individual contributions to $F_{\text{total}}^{\text{exp}}$ are gravitational force F_g , ion drag force F_i and electric field force F_f . The shown F_i for a particle with $q = -10^5 e_0$ is an upper bound estimate of this contribution. F_f is calculated for various positive particle charges using the PIC results for the electric field. Upper right panel: collection radius b_c and Coulomb scattering radius b_s for different particle charges q as derived from the PIC data in the lower panel. Curves and legend correspond from top to bottom. Lower panel: PIC results for ion density n_i , ion thermal velocity v_i^{th} and ion drift velocity v_i above the center pixel of the AE for bias configuration $U_{\text{AE}}[\text{V}] = (-20, -20, -50)$.

experimental trajectory, we performed a polynomial fit to the measured data (inset of Fig. 5) and calculated its second derivative. Due to the limited number of data points, the curvature data depend slightly on the order of the used polynomial, but they agree within 5% in the relevant time interval. Combining trajectory and time dependent force data, the total force on the particle is given as a function of distance above the AE in the upper panel of Figure 9. Gravity is responsible for only about 10% of the observed particle acceleration. Also the ion drag force, which presumably becomes enhanced by the negative pixel biasing, contributes to the acceleration. It is given by

$$F_i = m_i n_i v_i \bar{v}_i (\pi b_c^2 + \pi b_s^2 \ln A), \quad (3)$$

where m_i , n_i , v_i are the ion mass, density and drift velocity. Accounting for the thermal motion of the ions, we define the effective velocity $\bar{v}_i^2 = v_i^2 + (v_i^{\text{th}})^2$, where v_i^{th} is the thermal ion velocity. In (3), the two contributions to the ion drag force correspond to momentum transfer due to collection of ions (index c) and Coulomb scattering (index s). The radii in the associated cross sections are given by [4]

$$b_c = \frac{d}{2} \sqrt{1 - \frac{2e_0 \Phi_d}{m_i \bar{v}_i^2}} \quad \text{and} \quad b_s = \frac{e_0 q}{2\pi \epsilon_0 m_i \bar{v}_i^2}, \quad (4)$$

where Φ_d is the potential of the dust particle, and ϵ_0 the permittivity of vacuum. The divergence of the

Coulomb scattering cross section is circumvented by using a suitable cutoff beyond which passing ions are neglected [4,22,24,25]. The shielding effect of the plasma suggests [24] to use the electron Debye length $\lambda_D = [(\epsilon_0 k_B T_e)/(n_e e_0^2)]^{1/2}$ as cutoff, leading to the approximate Coulomb logarithm $\ln A \approx \ln(2\lambda_D/d)$. Treating the dust particle as a spherical capacitor, its potential and charge are related by $\Phi_d = q/C$ with $C = 2\pi\epsilon_0 d(1 + d/(2\lambda_D))$.

Evaluating (3) requires knowledge about ion density and velocities in the sheath. These quantities are directly accessible by PIC and are shown in the lower panel of Figure 9. Alternatively, the sheath parameters can be estimated from Child's law [4]. The large dc-bias applied to the AE pixel locally dominates the characteristics of the sheath and masks the rf-character of the global discharge there. Low pressure should permit the neglect of ion collisions in the sheath and due to the additional bias the sheath potential is much larger than the electron temperature. Yet, within Child's law the sheath width is less than half the width of the PIC solution, with similar density and velocity profiles on this reduced scale. We attribute this discrepancy to the local character of the disturbance of the plasma conditions by the pixel biasing. Using the PIC data, we may calculate the two contributions to the ion drag force for different particle charges (see upper right panel of Fig. 9). The bias switching enlarges the sheath instantaneously (within 1–5 rf-cycles). Therefore the initial particle position is already deep inside the sheath. Irrespective of the particle charge, the collection radius b_c in this region essentially coincides with the particle radius. Only extremely high charges ($q \sim -10^5 e_0$) can compensate the high ion velocity resulting in a noticeable second term under the square root in (4). The proportionality of the Coulomb scattering radius b_s to the particle charge often results in a dominance of b_s over b_c . In the relevant region, however, the high values of \bar{v}_i result in a small prefactor and b_c and b_s become comparable for $q \sim -5 \times 10^4 e_0$. Summing up both contributions, the resulting ion drag force for $q = -10^5 e_0$ is given in the upper left panel of Figure 9. Due to the quadratic dependence of F_i on b_c and b_s , the curves for smaller q are marginal on this scale. In order to explain the remaining difference to the measured total force, the only explanation seems to be a positive recharging of the particle. The resulting electric field forces for selected positive charges are given in left panel of Figure 9. An explanation of the observed behavior requires a gradual charging to $q \sim 2.5 \times 10^4 e_0$ during the fall. Crucial for this recharging procedure are: (i) absence of any electrons in the vicinity of the particle during the whole rf-cycle, which is guaranteed by the large negative pixel biasing; (ii) instantaneous sheath widening and location of the particle deep inside the widened sheath. Then the accelerated ions may acquire high enough energies to reach the particle surface, even for a positively charged particle.

Experiments for which these findings might be of relevance range from dusty plasmas to several technological plasma processing environments. Arcing and sudden surface charging have been observed in physically enhanced

chemical vapor deposition processes or magnetron sputtering [26,27]. Similar conditions are important in plasma ion immersion implantation for surface treatment [28,29], where an ion matrix sheath is created by an abrupt negative high-voltage pulse that is used to accelerate the ions for implantation. In both cases, the results of our studies will apply to microparticles (dust, flakes, powders etc.) that are present in those discharges.

4 Conclusions

In this work, we studied the behavior of a microparticle upon local perturbations of the plasma sheath above biased segments of an ‘adaptive electrode’, and upon abrupt changes of the local plasma conditions. In order to obtain a better understanding of the phenomena, experimental studies are combined with theoretical modeling and numerical simulations. Hereby, special emphasis is put on the particle dynamics upon bias switching and in the afterglow of the discharge.

Whether a particle drops onto the adaptive electrode or relaxes into another equilibrium position depends on the charge equilibrium imposed by the altered plasma conditions in its vicinity and the ordering of time scales. Relaxation into a new equilibrium position is a markedly slower process than the adaption of the particle charge to the local electron and ion densities. Slight changes of the plasma conditions initiate a damped oscillation of the particle into a new equilibrium position. In the temporal afterglow of the discharge, the particle remains hovering above a biased segment of the electrode if the retained biasing is sufficiently large.

Above a critical bias, the particle is subject to an additional downward acceleration that is not explicable solely by gravity and the ion drag force. Alike, for bias switching experiments, a too large bias difference induces an accelerated fall of the particle. The additional acceleration can be explained by a positive recharging of the particle that may arise since locally the sheath is deprived completely of electrons due to the large negative bias. Under such extreme local out-of-equilibrium conditions, the particle’s charge balance may be disturbed to the point of a significant positive recharging in a locally biased plasma sheath and its afterglow. In the presence of microparticles, these effects are also of relevance for technological plasma processes like physically enhanced chemical vapor deposition, magnetron sputtering and plasma ion immersion implantation.

To conclude, the utilization of charged test particles in locally tailored plasma sheath environments is a promising method for the characterization of electric field structures and plasma density profiles.

This work has been supported by the Deutsche Forschungsgemeinschaft under SFB-TR 24, projects A5 and B4. We would like to thank F.X. Bronold, K. Matyash and R. Schneider for helpful discussions.

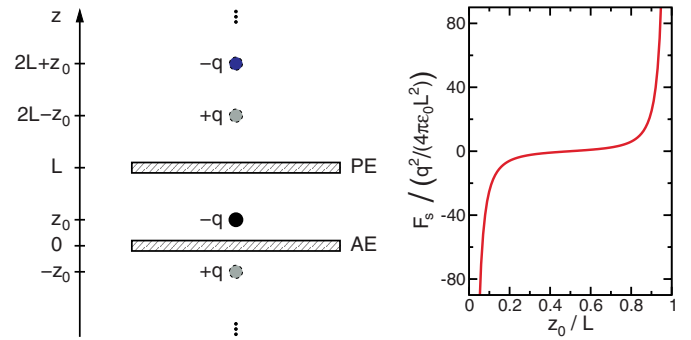


Fig. A.1. (Color online) Left panel: construction of image charges to calculate the force on a charged particle (black) between two parallel, grounded electrodes. Starting with the AE, an image charge of opposite sign (light grey) is constructed at $z = -z_0$. To describe the effect of the PE, image charges for both the original and the first image charge have to be constructed at $z = 2d \pm z_0$. These steps have to be iterated and generate an infinite series of image charges by repeatedly reflecting the newly created image charges at the AE and PE. The force acting on the original charge is then calculated from Coulomb’s law accumulating contributions from all charges. Right panel: Force on a particle between two parallel grounded plates as a function of distance from the electrode.

Appendix A: Particle self-force

Summing up the contributions of all image charges in Figure A.1, we get

$$F_s = \frac{q^2}{4\pi\epsilon_0} \left(\frac{-1}{4z_0^2} + \sum_{j=0}^{\infty} \frac{(-1)^j}{(z_0 - r_j)^2} \right), \quad (\text{A.1})$$

with $r_j = (-1)^{\lfloor j/2 \rfloor} (2L(\lfloor j/4 \rfloor + 1) + (-1)^{j+1} z_0)$, where the floor function $\lfloor \cdot \rfloor$ returns the largest integer that is not greater than its argument, e.g., $\lfloor 1.75 \rfloor = 1$. The infinite sum in (A.1) may be evaluated and with $x = z_0/L$ and the trigamma function $\psi_1(x) = \sum_{j=0}^{\infty} 1/(x+j)^2$ we get

$$F_s = \frac{q^2}{4\pi\epsilon_0 L^2} \left(\frac{\pi^2}{4} (1 + \cot(\pi x)) - \frac{1}{2} \psi_1(x) \right). \quad (\text{A.2})$$

In the right-hand panel of Figure A.1 we show F_s as a function of distance from the AE. For the relevant parameters ($L = 10$ cm, $q \sim 10^4 e_0$) the prefactor in (A.2) is six orders of magnitude smaller than the gravitational force acting on the considered particle. Thus, F_s is negligible except for the vicinity of the electrodes at which (A.2) diverges. For the above parameters gravity and F_s become comparable for $z_0 \sim 0.05$ mm.

Appendix B: Details on PIC simulation

All presented simulation results have been calculated using an electrostatic $2d(r, z)3v$ PIC code. Since simulating the whole reactor vessel is infeasible, we restricted the simulation volume to the relevant region above the AE ($L_z = 5$ cm, $r_{\max} = 6$ cm). By suitable choice of the substitute

discharge parameters we ensured bulk plasma conditions in accordance with the experimental ones, $\Phi_p = 21.8$ V, $T_e = 1.1$ eV, $n_e = 2.5 \times 10^9$ cm $^{-3}$. While the obtained plasma potential and densities deviate from their target values less than 1%, they are slightly larger for the electron temperature.

Adopting the general code structure and null-collision method [30,31] from the xdp2 code suite, [32,33] our code has been tailored to match the specific requirements: rotational symmetry, inclusion of the AE, individual particle weighting, OpenMP-parallelization). The neglect of Coulomb collisions between charged species can be justified by the low degree of ionization ($n_e/n_{Ar} \sim 10^{-5}$) for the considered experimental conditions. Thermal motion of the fixed background gas is taken fully into account for ion neutral collisions while being neglected for electron neutral collisions due to the large mass ratio and thus faint momentum transfer. The solution of the Poisson equation is performed by means of Fourier accelerated cyclic reduction [34] as implemented, e.g., in FISHPACK [19]. We ensured numerical stability of our results for the considered grid sizes ($n_z \times n_r = 1000 \times 1200$) by using double precision variables for the potential and charge density. The constant grid spacing of $\Delta_r = \Delta_z = 0.05$ mm is smaller than half the Debye length. By choosing a time step of $\Delta t = 2.83 \times 10^{-11}$ s we ensure $\omega_p \Delta t < 1/5$, where ω_p is the plasma frequency. Respecting these constraints, the PIC method provides reliable results [35]. Modeling a vertical cut through the reactor vessel, symmetry implies a vanishing electric field at the inner boundary, $r = 0$, of the simulation volume. At the outer boundary, $r = r_{max}$, we assume vanishing electric field boundary conditions since the lateral dimension of the simulation volume covers only a fraction of the powered electrode. In order to model the AE, each pixel has been associated to an individual external circuit, and the charge balance is calculated in each iteration. A linear weighting scheme for particle deposition to the grid and interpolation of the electric field ensures conservation of momentum and absence of self-forces. The r -dependence of the volume elements in cylindrical coordinates leads to a drastically varying number of superparticles in each cell when describing a constant density. Alternatively, additional weighting factors for each superparticle may compensate for this [36]. Thereby, the statistics can be markedly improved since the initial number of superparticles in all cells is balanced. Throughout this work we used a mean number of superparticles per cell of $\langle N_c \rangle \approx 80$. Note that these individual weighting factors have to remain constant during the whole simulation in order to ensure conservation of energy and momentum and absence of self-forces. As a consequence of the experimental setup, the main particle motion is in z -direction. Radially, the particles remain within nearby cells of their initial position. Thus, we are in the lucky position that the statistical advantage due to the individual weighting decays only slowly with time.

In the experiment the AE-biasing does not influence the global discharge parameters but only locally disturbs the plasma sheath. This behavior reflects the small ratio

of biased electrode to wall surface. The restricted size of the simulation volume implies a more pronounced impact of the AE-pixels on the bulk plasma due to the larger surface ratio. Nevertheless, the numerical bulk quantities with and without AE-biasing differ only by around 1%.

References

1. L. Boufendi, A. Bouchoule, Plasma Source. Sci. Technol. **11**, A211 (2002)
2. H. Kersten, G. Thieme, M. Fröhlich, D. Bojic, H.T. Tung, M. Quaas, H. Wulff, R. Hippler, Pure Appl. Chem. **77**, 415 (2005)
3. K.N. Ostrikov, S. Kumar, H. Sugai, Phys. Plasmas **8**, 3490 (2001)
4. M.A. Lieberman, A.J. Lichtenberg, *Principles of plasma discharges and materials processing*, 2nd edn. (John Wiley & Sons, Hoboken, New Jersey, 2005)
5. M.E. Koepke, N. Sato, New J. Phys. **5**, 42 (2003)
6. U. Czarnetzki, G.A. Hebner, D. Luggenhölscher, H.F. Döbele, M.E. Riley, IEEE Trans. Plasma Sci. **27**, 70 (1999)
7. U. Czarnetzki, D. Luggenhölscher, V. Kadetov, H.F. Döbele, Pure Appl. Chem. **77**, 34 (2005)
8. B.M. Annaratone, M. Glier, T. Stuffer, M. Raif, H.M. Thomas, G.E. Morfill, New J. Phys. **5**, 92 (2003)
9. R. Basner, F. Sigeneger, D. Loffhagen, G. Schubert, H. Fehske, H. Kersten, New J. Phys. **11**, 013041 (2009)
10. A.A. Samarian, B.W. James, Plasma Phys. Control. Fusion **47**, B629 (2005)
11. H. Kersten, H. Deutsch, M. Otte, G.H.P.M. Swinkels, G.M.W. Kroesen, Thin Solid Films **377/378**, 530 (2000)
12. L. Couëdel, M. Mikikian, L. Boufendi, A.A. Samarian, Phys. Rev. E **74**, 026403 (2006)
13. G. Thieme, R. Basner, R. Wiese, H. Kersten, Faraday Discuss. **137**, 157 (2008)
14. M. Tatanova, G. Thieme, R. Basner, M. Hannemann, Y.B. Golubovskii, H. Kersten, Plasma Source. Sci. Technol. **15**, 507 (2006)
15. S. Epstein, Phys. Rev. **23**, 710 (1924)
16. Y. Nakamura, O. Ishihara, Rev. Sci. Instrum. **79**, 033504 (2008)
17. M.Y. Pustynnik, N. Ohno, S. Takamura, R. Smirnov, Phys. Rev. E **74**, 046402 (2006)
18. J.D. Jackson, *Classical Electrodynamics*, 3rd edn. (John Wiley & Sons, New York, 1998)
19. J. Adams, P. Swartztrauber, R. Sweet, *FISHPACK – efficient FORTRAN subprograms for the solution of separable elliptic partial differential equations*, <http://www.cisl.ucar.edu/css/software/fishpack>
20. K. Matyash, R. Schneider, J. Plasma Phys. **72**, 809 (2006)
21. M. Osiac, T. Schwarz-Selinger, D. O’Connell, B. Heil, Z. Petrovic, M.M. Turner, T. Gans, U. Czarnetzki, Plasma Source. Sci. Technol. **16**, 355 (2007)
22. M.S. Barnes, J.H. Keller, J.C. Forster, J.A. O’Neill, D.K. Coultas, Phys. Rev. Lett. **68**, 313 (1992)
23. S.V. Vladimirov, V.N. Tsytovich, Phys. Rev. E **58**, 2415 (1998)
24. S.V. Vladimirov, N.F. Cramer, Phys. Rev. E **62**, 2754 (2000)
25. S.A. Khrapak, A.V. Ivlev, G.E. Morfill, H.M. Thomas, Phys. Rev. E **66**, 046414 (2002)
26. A. Garscadden, B.N. Ganguly, P.D. Haaland, J. Williams, Plasma Source. Sci. Technol. **3**, 239 (1994)

27. I. Safi, Surf. Coat. Technol. **127**, 203 (2000)
28. J. Brutscher, R. Günzel, W. Möller, Plasma Source. Sci. Technol. **5**, 54 (1996)
29. S. Mändl, R. Günzel, W. Möller, J. Phys. D **31**, 1109 (1998)
30. C. Birdsall, IEEE Trans. Plasma Sci. **19**, 65 (1991)
31. V. Vahedi, M. Surenda, Comput. Phys. Commun. **87**, 179 (1995)
32. V. Vahedi, C.K. Birdsall, M.A. Liebermann, G. DiPeso, T.D. Rognlien, Phys. Fluids B **5**, 2719 (1993)
33. V. Vahedi, G. DiPeso, J. Chem. Phys. **131**, 149 (1997)
34. P. Swarztrauber, SIAM Rev. **19**, 490 (1977)
35. D. Tskhakaya, K. Matyash, R. Schneider, F. Taccogna, Contrib. Plasma Phys. **47**, 563 (2007)
36. C. Soria-Hoyo, F. Pontiga, A. Castellanos, J. Phys. D **41**, 205206 (2008)